

List of Figures

Chapter 1 Introduction

Fig. 1.1 Unit cell of α -Ti.	13
Fig. 1.2 Unit cell of β -Ti.	14
Fig. 1.3 Effect of alloying elements on phase diagrams of titanium alloys (schematically).	15
Fig. 1.4 Schematic of a vacuum casting furnace used for making titanium castings.	16
Fig. 1.5 Low-yttria portion of proposed ZrO_2 - Y_2O_3 phase diagram. ...	17

Chapter 2

Ti₂ZrO Phases Formed in the Titanium and Zirconia Interface after Reaction at 1550°C

Fig. 2.1 (a) The TEM micrograph showing the interface between Cp-Ti and $ZrO_2(3Y)$ after reaction at 1550 °C /30min; (b) A magnified micrograph of the marked region in (a), indicating elongated β' -Ti and the lamellar structure of α -Ti and Ti_2ZrO in both sides of β' -Ti. The arrows in the lower right region indicate the spherical ordered Ti_2ZrO	30
Fig. 2.2 (a) and (b) SADP's of β' -Ti, $Z=[110]_{\beta'-Ti}$ and $Z=[111]_{\beta'-Ti}$, respectively ; (c) EDS of β' -Ti.	31
Fig. 2.3 (a) SADP's of the lamellar Ti_2ZrO and α -Ti, $Z=[0001]_{\alpha-Ti}$	

// $[110]_{\text{Ti}_2\text{ZrO}}$; (b) EDS of α -Ti; (c) EDS of the lamellar Ti_2ZrO ; (d) the standard stereographic projection with $[0001]_{\alpha\text{-Ti}} // [110]_{\text{Ti}_2\text{ZrO}}$32

Fig. 2.4 The lattice relation of the orthorhombic Ti_2ZrO (dash line) and hexagonal α -Ti (soild line).33

Fig. 2.5 (a) SADP's of the spherical ordered Ti_2ZrO and α -Ti, $Z=[0001]_{\alpha\text{-Ti}} // [0001]_{\text{Ti}_2\text{ZrO}}$; (b) the hexagonal Ti_2ZrO unit cell ¹⁷; (c) EDS of the spherical ordered Ti_2ZrO ; (d) the standard stereographic projection with $[0001]_{\alpha\text{-Ti}} // [0001]_{\text{Ti}_2\text{ZrO}}$34

Chapter 3

Zirconia-Related Phases in the Zirconia/Titanium Diffusion Couple after Annealing at 1100° to 1550°C

Fig. 3.1 (a) TEM micrograph (bright field image, BFI) of zirconia far away the ZrO_2/Ti interface after reaction at 1100°C/6 h, indicating $t\text{-ZrO}_{2-x}$ with an average grain size $\sim 0.5 \mu\text{m}$; (b) SADP of the $t\text{-ZrO}_{2-x}$51

Fig. 3.2 SEM micrograph (backscattered electron image, BEI) of the zirconia side in the ZrO_2/Ti diffusion couple after reaction at 1300°C/6 h, indicating the coexistence of $\alpha\text{-Zr}$ (marked as “A”) and $t\text{-ZrO}_{2-x}$, (marked as “B”). Also shown is the coarsening of $\alpha\text{-Zr}$ (arrowed).52

Fig. 3.3 (a) TEM micrograph (bright field image, BFI) of $\alpha\text{-Zr}$ and $t\text{-ZrO}_{2-x}$ in the ZrO_2/Ti diffusion couple after reaction at 1300°C/6 h; (b) SADP of the $\alpha\text{-Zr}$ along the $[101]$ zone axis; (c) EDS of the $\alpha\text{-Zr}$ shown in (b); (d) SADP of the $t\text{-ZrO}_{2-x}$, along the $[110]$ zone axis; (e) EDS of the $t\text{-ZrO}_{2-x}$ shown in (d).53

Fig. 3.4 (a) SEM micrograph (backscattered electron image, BEI) of zirconia side in the ZrO_2/Ti diffusion couple after reaction at $1550^\circ C/6$ h, indicating the coarsening of intergranular α -Zr (marked as “A”) and t - ZrO_{2-x} (marked as “B”) in the c - ZrO_{2-x} matrix (marked as “C”); (b) SEM micrograph (secondary electron image, SEI) of as hot-pressed zirconia after annealing at $1550^\circ C/6$ h in Ar.54

Fig. 3.5 (a) TEM micrograph (bright field image, BFI) of zirconia in the ZrO_2/Ti diffusion couple after reaction at $1550^\circ C/6$ h, indicating the twined t' - ZrO_{2-x} in t' - ZrO_{2-x} matrix; (b) and (c) are microdiffraction patterns from the twined t' - ZrO_{2-x} and the t' - ZrO_{2-x} matrix along the zone axes of $[111]$, respectively.55

Fig. 3.6 (a) TEM micrograph (bright field image, BFI) of zirconia in the ZrO_2/Ti diffusion couple after reaction at $1550^\circ C/6$ h, displaying $\{100\}$ type of variants of the lenticular t - ZrO_{2-x} in c - ZrO_{2-x} matrix; (b) A magnified image of the c - ZrO_{2-x} matrix in (a), showing the ordered structure; (c) EDS of the ordered c - ZrO_{2-x} ; (d) and (e) are SADP's of the ordered c - ZrO_{2-x} matrix with zone axis being $[110]$ and $[310]$, respectively.56

Fig. 3.7 Schematic diagrams showing the microstructural evolution of the zirconia side in the ZrO_2/Ti diffusion couple annealed at $1300^\circ C/6$ h. (a) as hot-pressed; (b) grain growth on heating to $1300^\circ C$; (c) exclusion of α -Zr from ZrO_{2-x} during cooling.57

Fig. 3.8 Schematic diagrams showing the microstructural evolution of the zirconia side in ZrO_2/Ti diffusion couple annealed at $1550^\circ C/6$ h. (a) as hot-pressed; (b) apparent grain growth on heating to $1550^\circ C$; (c) exclusion of α -Zr during cooling; (d) formation of twined t' - ZrO_2 ; (e) the formation of lenticular t - ZrO_2 and ordered c - ZrO_{2-x}

during cooling.58

Chapter 4

Microstructural Evolution and Formation Mechanism of the Interface between Titanium and Zirconia Annealed at 1550°C

Fig. 4.1 (a), (b), and (c) SEM micrographs (backscattered electron image, BEI) of the cross-sectional between Ti/ZrO₂ after reaction at 1550°C/0.5 h, 3h, and 6h, respectively. The arrows indicated the interface between Ti/ZrO₂.77

Fig. 4.2 (a) SEM micrograph (backscattered electron image, BEI) of the cross-sectional between Ti/ZrO₂ after reaction at 1550°C/6 h; (b)~(e) X-ray maps of Y, Ti, Zr, and O, respectively.78

Fig. 4.3 SEM micrograph (backscattered electron image, BEI) of the reaction layers “A”, “B”, and “C” in the interface between Ti/ZrO₂ after reaction at 1550°C/6 h.79

Fig. 4.4 SEM micrograph (backscattered electron image, BEI) of the reaction layer “D” in the interface between Ti/ZrO₂ after reaction at 1550°C/6 h.80

Fig. 4.5 (a) TEM micrograph (bright field image, BFI) of the cross-sectional between Ti/ZrO₂ after reaction at 1550°C/6 h; (b) and (c) selected area diffraction patterns of the α -Ti and β' -Ti, $Z=[2\bar{1}\bar{1}0]_{\alpha\text{-Ti}} // [001]_{\beta'\text{-Ti}}$ and its schematic diagram (Δ : α -Ti, \circ : β' -Ti), respectively; (d) and (e) energy-dispersive spectra of α -Ti and β' -Ti.81

Fig. 4.6 (a)TEM micrograph (bright field image, BFI) of the

cross-sectional between Ti/ZrO₂ after reaction at 1550°C/6 h; (b) and (c) selected area diffraction patterns of the α-Ti and β'-Ti, $Z=[2\bar{1}\bar{1}0]_{\alpha\text{-Ti}} // [021]_{\beta'\text{-Ti}}$ and its schematic diagram (Δ : α-Ti, \circ : β'-Ti), respectively; (d) images taken from the high resolution transmission electron microscopy (HRTEM) of acicular α-Ti and β'-Ti; (e) the computer simulation in the marked area of Fig. 4.3(d).82

Fig. 4.7 SEM micrograph (backscattered electron image, BEI) of the reaction layers “D”, “E”, and “F” in the interface between Ti/ZrO₂ after reaction at 1550°C/6 h.83

Fig. 4.8 (a) SEM micrograph (backscattered electron image, BEI) of the reaction layers “F” in the interface between Ti/ZrO₂ after reaction at 1550°C/6 h; (b)~(e) X-ray maps of Y, Ti, Zr, and O, respectively.84

Fig. 4.9 (a) SEM micrograph (backscattered electron image, BEI) of the reaction layer “G” in the zirconia side away from the interface after reaction at 1550°C/6 h; (b)~(e) X-ray maps of Y, Ti, Zr, and O, respectively.85

Fig. 4.10 Schematic diagrams showing the microstructural evolution of the Ti/ZrO₂ diffusion couple annealed at 1550°C. (a) as hot-pressed; (b) the Ti-Zr-O ternary system at 1450°C¹⁹; (c) the structure of the Ti/ZrO₂ diffusion couple annealed at 1550°C, and (d) the structure on cooling.86

Chapter 5

Temperature Dependence of the Interfacial Reaction between Titanium and Zirconia Annealed between 1100° and 1550°C

Fig. 5.1 SEM micrographs (backscattered electron image) showing the interface of Ti and ZrO₂ after reaction for 6 h at (a) 1100°; (b) 1300°; (c) 1400°; and (d) 1550°C. The vertical arrows in the upper side indicated the original interface. The interface reaction layers were designed as the layers “I”, “II”, “III”, “IV”, “V”, and “VI,” respectively.108

Fig. 5.2 SEM micrographs (secondary electron image) showing the variation of the layer “I” after reaction at (a) 1300°; (b) 1400°; and (c) 1550°C, respectively.109

Fig. 5.3 (a) A TEM micrograph (bright field image, BFI) showing the layer “I” with the coexistence of α -Ti and Ti₂ZrO after reaction at 1100°C/6 h; (b) selected area diffraction patterns of the α -Ti and Ti₂ZrO, indicating that $[0001]_{\alpha\text{-Ti}} // [110]_{\text{Ti}_2\text{ZrO}}$ and $(10\bar{1}0)_{\alpha\text{-Ti}} // (1\bar{1}0)_{\text{Ti}_2\text{ZrO}}$ (A = $(01\bar{1}0)_{\alpha\text{-Ti}}$, B = $(10\bar{1}0)_{\alpha\text{-Ti}}$, C = $(00\bar{2})_{\text{Ti}_2\text{ZrO}}$, D = $(1\bar{1}0)_{\text{Ti}_2\text{ZrO}}$); (c) the energy-dispersive spectrum of Ti₂ZrO.110

Fig. 5.4 TEM micrograph (bright field image, BFI) of the layer “II” showing the lamellae α -Ti + Ti₂ZrO and β' -Ti after reaction at 1550°C for 6 h; the inset selected area diffraction patterns indicate $[0001]_{\alpha\text{-Ti}} // [110]_{\text{Ti}_2\text{ZrO}}$ and $(10\bar{1}0)_{\alpha\text{-Ti}} // (1\bar{1}0)_{\text{Ti}_2\text{ZrO}}$ (A = $(01\bar{1}0)_{\alpha\text{-Ti}}$, B = $(10\bar{1}0)_{\alpha\text{-Ti}}$, C = $(00\bar{2})_{\text{Ti}_2\text{ZrO}}$, D = $(1\bar{1}0)_{\text{Ti}_2\text{ZrO}}$); (c) the energy-dispersive spectrum of Ti₂ZrO.111

Fig. 5.5 TEM micrograph (bright field image, BFI) of the reaction layer “III” showing the coexistence of β' -Ti and α -Ti after reaction at (a) 1400°C/6 h (A = $(0001)_{\alpha\text{-Ti}}$, B = $(01\bar{1}0)_{\alpha\text{-Ti}}$, C = $(\bar{1}\bar{1}0)_{\beta'\text{-Ti}}$, and D = $(\bar{1}10)_{\beta'\text{-Ti}}$) in the inset selected area diffraction pattern (SADP) and (b) 1550°C/6 h (A = $(0001)_{\alpha\text{-Ti}}$, B = $(01\bar{1}0)_{\alpha\text{-Ti}}$, C = $(\bar{1}1\bar{2})_{\beta'\text{-Ti}}$, and D = $(11\bar{2})_{\beta'\text{-Ti}}$) in the insert SADP).112

Fig. 5.6 TEM micrograph (bright field image, BFI) of the reaction layer

“V” consisting of β' -Ti and c -ZrO_{2-x} after reaction at (a) 1400°C/6 h; (b) at 1550°C/6 h; (c) a selected area diffraction pattern (SADP) of β' -Ti in Fig. 5.6(b) (Zone axis is [021], A = ($\bar{2}$ 00), B = ($\bar{2}$ 2 $\bar{2}$), and C = ($\bar{1}$ 1 $\bar{1}$)); (d) a SADP of β' -Ti in Fig. 5.6(b) (Zone axis is [$\bar{1}$ 12], A = ($\bar{1}$ 3 $\bar{2}$), B = ($\bar{1}$ 10), and C = ($\bar{1}$ 1 $\bar{1}$)).113

Fig. 5.7 TEM micrograph (bright field image, BFI) of the layer “VI” far away from the interface after reaction at (a) 1100°C, (b) 1300°C, (c) 1400°C, and (d) 1550°C for 6h.114

Fig. 5.8 (a) TEM micrograph (bright field image, BFI) of the suboxide Ti₃O near the reaction layer “I” after reaction at 1550°C for 6 h; (b) the energy-dispersive spectrum of Ti₃O; (c) the selected area diffraction pattern (SADP) along the [$2\bar{1}\bar{1}0$] zone axis (A = (0002) and B = (0 $\bar{1}$ 11)); (d) a SADP of Ti₃O along the [$1\bar{1}00$] zone axis. (A = (0002), B = (11 $\bar{2}$ 0), C = ($\frac{1}{3}$ $\frac{1}{3}$ $\frac{2}{3}$ $\frac{1}{2}$), and D = ($\frac{2}{3}$ $\frac{2}{3}$ $\frac{4}{3}$ $\frac{1}{2}$)).115

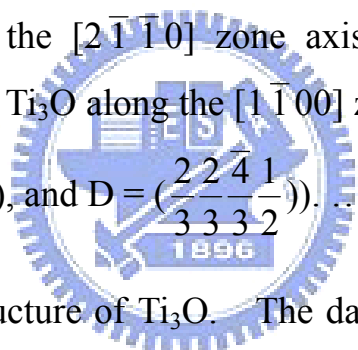


Fig. 5.9 The crystal structure of Ti₃O. The dash line indicates that the Ti₃O structure is based on the Ti₂O structure (solid line). ⊙: oxygen position, ●: titanium position, ●: unoccupied oxygen position.¹⁵116

Fig. 5.10 Schematic diagrams showing the microstructural evolution of the Ti/ZrO₂ diffusion couple annealed at 1550°C. (a) as hot-pressed; (b) the relation between the Ti-Zr-O phase diagram.²⁰; (c), (d), and (e) the microstructure of Ti/ZrO₂ diffusion couple on annealing at 1300°, 1400°, and 1550°C and their cooling stages, respectively.117